

# Micromagnetic simulation of dynamic and thermal effects

T. Schrefl, J. Fidler, D. Suess, W. Scholz, V. Tsiantos  
Institute of Applied and Technical Physics  
Vienna University of Technology  
Wiedner Haupstr. 8-10  
A-1040 Wien

## Contents

List of symbols.....	
1. Introduction.....	
2. Micromagnetic background.....	
2.1. Equation of motion.....	
2.2. Gibbs free energy.....	
2.3. Langevin dynamics .....	
2.4. Characteristic length scales.....	
3. Numerical techniques	
3.1. Finite element discretization.....	
3.2. Magnetostatic field calculation .....	
3.3. Time integration.....	
4. Numerical examples	
4.1. Small particles.....	
4.2. Thin film elements	
4.3. Circular nano-dots	
4.4. Magnetic nano-wires	

## List of Symbols

$\alpha$	Gilbert damping constant
$\gamma$	gyromagnetic ratio
$\delta_0$	Bloch parameter
$\delta_N$	Neel wall width
$\delta_w$	Bloch wall width
$\mu_0$	permeability of vacuum
$\tau$	relaxation time
$\omega$	Lamor frequency
$A$	exchange constant
$d$	nano-dot diameter
$E$	total magnetic Gibbs free energy
$E_B$	energy barrier

$f_0$	attempt frequency
$f_k$	magneto-crystalline anisotropy energy density
$\mathbf{H}_d$	demagnetizing field
$\mathbf{H}_{\text{eff}}$	effective magnetic field
$\mathbf{H}_{\text{ext}}$	external magnetic field
$H_K$	effective anisotropy field
$H_{th,i}^{(k)}$	$i$ -th component of the thermal fluctuation field at magnetic moment $k$
$k_B$	Boltzmann constant
$K$	effective anisotropy constant
$K_u$	uniaxial anisotropy constant
$l_{\text{ex}}$	exchange length
$\mathbf{M}$	magnetization
$\mathbf{m}$	magnetic moment
$M_s$	spontaneous magnetization
$M_z$	average magnetization parallel to the z-axis
$T$	temperature
$t$	nano-dot thickness
$v$	activation volume

## 1. Introduction

Small magnetic elements are the basic structural units of magneto-electronic devices (Prinz 1999) and discrete storage media (Terris et al. 1999). The development of magnetic sensors or magnetic memory cells requires a precise knowledge of the magnetization reversal mechanism of magnetic nano-structures. Finite element micromagnetics take into account the complex microstructure of magnetic materials such as edge roughness, grain structure, and particle shape. In combination with magnetic imaging using magnetic force (Dahlberg et al. 1995) and Lorentz (Kirk et al. 1997) microscopy, the simulations provide a useful tool to characterize the reversal magnetization reversal process. Both in magnetic recording and in magnetic memory cells as used in magnetic random access memories a high data rate is desired. Numerical micromagnetics can provide a basic understanding of the switching dynamics. If the particles are sufficiently small the magnetization reverses by quasi-uniform rotation (Street et al. 1999). Then the energy barrier for thermally activated switching decreases with decreasing particle volume. Thus with decreasing size of the structural magnetic units, thermal effects become important and may influence the switching time.

The time evolution of the magnetization can be computed by solving the Gilbert equation of motion (Gilbert 1955). It describes the precession of the magnetization around the effective magnetic field subject to viscous damping. The strength of the damping term considerably influences the reversal process (Kikuchi 1956). Kikuchi derived the critical value of the damping constant which minimizes the switching time. The Gilbert damping constant for critical damping is  $\alpha = 1$  for spheres and  $\alpha = 0.01$  for thin films. In order to include thermal activation a random thermal field can be added to

the effective field. The resulting stochastic equation of motion describes the random motion of the magnetization in thermal equilibrium and eventually across energy barriers.

Section 2 of this chapter describes the micromagnetic background of the simulations. Section 3 introduces the basic numerical techniques. Section 4 presents examples of the switching dynamics and thermal processes in columnar grains, thin film elements, nano-dots, and nano-wires.

## 2. Micromagnetic background

### 2.1. Equation of motion

The theoretical treatment of dynamic effects starts from the torque,  $\mathbf{m} \times \mathbf{H}_{\text{eff}}$ , exerted on the magnetic moment  $\mathbf{m}$ , by the effective field  $\mathbf{H}_{\text{eff}}$ . This torque will rotate the magnetic moments of the electrons with respect to the lattice. According to quantum theory the angular momentum associated with the magnetic moment  $\mathbf{m}$  is  $\mathbf{m}/\gamma$ , where  $\gamma$  is the gyromagnetic ratio of the system, often close to that of a free electron. The torque equation

$$\frac{\partial}{\partial t} \left( \frac{\mathbf{m}}{\tilde{a}} \right) = \mathbf{m} \times \mathbf{H}_{\text{eff}} \quad (1)$$

describes the motion of the magnetic moment around the effective field. Equation (1), which describes the gyromagnetic precession of the magnetic moment, states that the rate of change of the angular momentum with time,  $t$ , equals the torque.

In equilibrium the change of the angular momentum with time and thus the torque is zero. In order to describe the motion of the magnetic moment towards equilibrium a viscous damping term can be included. It results from a dissipative term,  $-\mathbf{h}(\partial\mathbf{m}/\partial t)$ , which is added to the effective field. This dissipative term is proportional to the generalized velocity,  $\partial\mathbf{m}/\partial t$ , with  $\mathbf{h}$  being a positive constant. The Gilbert equation of motion is

$$\frac{\partial}{\partial t} \left( \frac{\mathbf{m}}{\tilde{a}} \right) = \mathbf{m} \times \left( \mathbf{H}_{\text{eff}} - \mathbf{h} \frac{\partial\mathbf{m}}{\partial t} \right). \quad (2)$$

Equations (1) and (2) keep  $|\mathbf{m}|$  constant. In a more convenient notation, the Gilbert equation is

$$\frac{\partial\mathbf{m}}{\partial t} = -g|\mathbf{m}| \times \mathbf{H}_{\text{eff}} + \frac{\mathbf{a}}{|\mathbf{m}|} \mathbf{m} \times \frac{\partial\mathbf{m}}{\partial t} \quad (3)$$

where the dimensionless Gilbert damping constant  $\mathbf{a} = -g\mathbf{h}|\mathbf{m}|$  has been introduced.

The first term in the right hand side of equation (3) describes the gyromagnetic precession and the second term is the damping term which describes the motion of the

magnetic moment towards the effective field. In equilibrium the magnetic moment is parallel to the effective field and the torque,  $\mathbf{m} \times \mathbf{H}_{\text{eff}}$ , vanishes. Fig. 1 summarizes the basic contributions to the effective field. It is the sum of the exchange field, the magnetostatic field, the anisotropy field, and the external field. The exchange field and the magnetostatic field introduce interactions between neighboring magnetic moments. At non-zero temperatures a random stochastic field may be included. The exchange field causes the neighboring magnetic moments to be aligned parallel to each other, the magnetostatic field breaks large magnetic particles into smaller magnetic domains, the anisotropy field causes the magnetic moments to be oriented along certain crystallographic directions, and the external field rotates the magnetization parallel to its own direction.

## 2.2. Gibbs free energy

In equilibrium the total magnetic Gibbs free energy reaches a local minimum. The total magnetic Gibbs free energy is the sum of the exchange energy, the magnetostatic energy, the magnetocrystalline anisotropy energy, and the Zeeman energy (Brown 1963). In a continuum theory, the direction of the magnetic moments is described by the magnetization vector  $\mathbf{M}$ .  $\mathbf{M}$  is the magnetic moment ( $\mathbf{m}$ ) per unit volume. The total energy of a ferromagnetic particle is a function of the magnetization distribution  $\mathbf{M}(\mathbf{r})$  and the external field  $\mathbf{H}_{\text{ext}}$ :

$$E(\mathbf{M}, \mathbf{H}_{\text{ext}}) = \int \left\{ \frac{A}{M_s^2} \sum_{i=1}^3 (\nabla M_i)^2 - \frac{m_0}{2} \mathbf{H}_d \cdot \mathbf{M} + f_k(\hat{\mathbf{i}}) - m_0 \mathbf{H}_{\text{ext}} \cdot \mathbf{M} \right\} dV, \quad (4)$$

where  $M_s$  is the spontaneous magnetization and  $M_i$  is the  $i$ -th component of the magnetization vector  $\mathbf{M}$ .  $A$  is the exchange constant and  $f_k$  the magneto-crystalline anisotropy energy density. The demagnetizing field,  $\mathbf{H}_d$ , can be expressed in terms of magnetic volume charges,  $\nabla \cdot \mathbf{M}$ , due to inhomogeneous magnetization distributions within the magnetic particle and magnetic surface charges,  $\mathbf{M} \cdot \mathbf{n}$ , at grain boundaries and free surfaces with unit surface normal  $\mathbf{n}$ . The effective field is the negative variational derivative of (4) with respect to the magnetization.

## 2.3. Langevin equation

The effects of thermal motions on a short time scale can be treated numerically adding a random thermal field to the effective field in equation (3). This leads to the Langevin equation

$$\frac{\partial \mathbf{m}}{\partial t} = -g |\mathbf{m}| \times (\mathbf{H}_{\text{eff}} + \mathbf{H}_{\text{th}}) + \frac{\mathbf{a}}{|\mathbf{m}|} \mathbf{m} \times \frac{\partial \mathbf{m}}{\partial t} \quad (5)$$

The random field,  $\mathbf{H}_{\text{th}}$ , describes the coupling of the magnetic system with a heat bath. It accounts for the interaction of the magnetic polarization with the microscopic degrees of freedom which causes the fluctuation of the magnetization distribution. The fluctuations are assumed to take place on a much faster time scale than intrinsic time

scale given by the gyromagnetic ratio and the effective field. The intrinsic time scale as given by the Gilbert equation of motion follows from the Larmor frequency

$$\mathbf{w} = -\mathbf{g}\mathbf{H}_{\text{eff}}. \quad (6)$$

The thermal field is assumed to be a Gaussian random process with the following statistical properties:

$$\langle H_{\text{th},i}^{(k)} \rangle = 0, \quad (7)$$

$$\langle H_{\text{th},i}^{(k)} H_{\text{th},j}^{(l)} \rangle = D \mathbf{d}_{ij} \mathbf{d}_{kl} \mathbf{d}(t-t'). \quad (8)$$

The average of the thermal field taken over different realizations vanishes in each direction  $i$  in space.  $k$  and  $l$  are position indices. The thermal field is uncorrelated in time and space. The strength of the thermal fluctuations follow from the fluctuation-dissipation theorem (Brown 1979):

$$D = \frac{2\alpha k_B T}{g|\mathbf{m}|}, \quad (9)$$

where  $k_B$  is the Boltzmann constant and  $T$  the temperature.

Fig. 2 compares the motion of the magnetization towards equilibrium for different damping and different temperatures. The figure gives the trace of the magnetic moment in the  $x, y$  plane. The effective field is constant and parallel to the  $z$ -axis of the Cartesian coordinate system. At high damping the magnetization rotates more directly towards the field direction, as the second term in equation (3) is dominant. When the precession term becomes dominant and the magnetization precesses several times around the field direction before it reaches equilibrium. In the case of low damping and non-zero temperature the magnetization moves randomly and eventually comes to thermal equilibrium.

#### 2.4. Characteristic length scales

The competitive effects of the different contributions to the effective field lead to characteristic length scales on which the magnetization changes its direction. To minimize the magnetostatic energy magnetic particles may break up into domains with different directions of the magnetization. Within the domain wall the magnetization changes its direction on a length which is comparable with

$$\mathbf{d}_B = \mathbf{p} \sqrt{\frac{A}{K_u}} = \mathbf{p} \mathbf{d}_0, \quad (10)$$

in hard magnetic materials with a uniaxial anisotropy constant  $K_u$  or with

$$\mathbf{d}_N = \mathbf{p} \sqrt{\frac{2A}{\mathbf{m}_0 M_s^2}} = \mathbf{p} l_{\text{ex}} \quad (11)$$

in soft magnetic thin film. Here  $\delta_0$  is the Bloch parameter and  $l_{\text{ex}}$  is the exchange length. The smaller of the two values defines a characteristic length: The magnetization is often assumed to be uniform within regions smaller than about one half of the characteristic length. The domain wall width differs from the characteristic length by a factor of  $\pi$ .

In numerical micromagnetic simulations the ferromagnetic particle is subdivided into smaller computational cells. Within each cell the magnetization is assumed to be uniform. Thus it is possible to associate a rigid magnetic moment to each cell. The time evolution of the magnetization follows from the solution of a coupled system of ordinary equations. Generally one equation of motion as given by (3) has to be solved for each computational cell. In order to resolve the transition of the magnetization between magnetic domains it is required that the size of the computation cells are smaller than one half of the characteristic length. If this condition is fulfilled, the numerical results are independent of the grid size (Rave et al. 1998).

### 3. Numerical techniques

#### 3.1. Finite element discretization

One possible technique to subdivide the magnetic structure into computational cells is the finite element method. It has the advantage that complex microstructures like edge irregularities and polyhedral grains can be modeled easily (Schrefl 1999). The discretization starts from the continuum expression for the total energy (4). The magnetization vector is interpolated with piecewise linear function on a tetrahedral finite element mesh. Adaptive refinement methods (Hertel et al. 1998, Scholz et al. 1999) keep the number of elements small while resolving the magnetization within domain walls. It is possible to assign a magnetic moment to each node of the finite element grid using a box scheme

$$\mathbf{m}^{(k)} = \int_{V^{(k)}} M_s(\mathbf{r}) dV, \quad (12)$$

where the integral is taken over the volume  $V^{(k)}$  surrounding node  $k$ . The box volumes fulfill the condition

$$\sum_k V^{(k)} = \int dV, \quad V^{(k)} \cap V^{(l)} = 0, \text{ for } k \neq l. \quad (13)$$

Fig. 3a gives an example for an adaptive finite element grid obtained from the simulation of domain wall motion in a thin specimen of a granular hard magnet (Scholz et al. 2000). Fig. 3b shows the schematics of the box scheme. The effective field at node  $k$ , can be approximated using

$$\mathbf{H}_{\text{eff}}^{(k)} = -\frac{\partial E}{\partial \mathbf{m}^{(k)}}. \quad (14)$$

With equation (4), (12), and (14) the magnetic moment and the effective field can be evaluated at the nodes of the finite element mesh. Now for each node an equation of

motion has to be solved. The equations at the different nodes are coupled by the exchange and magnetostatic field.

### 3.2. Magnetostatic field calculation

The exchange field and the magnetostatic field couple the motion of the magnetic moments at the nodes of the finite element grid. Whereas the exchange interaction is short range and involves only nearest neighbors, the magnetostatic interaction is long range. The demagnetizing field,  $\mathbf{H}_d$ , at a given node depends on the magnetization distribution over the entire mesh. On regular grids fast fourier transform methods (Ramstöck 1994) are used to effectively compute the magnetostatic interactions. The simulation of irregular grain structure require unstructured grids. It is possible to eliminate the long range terms from the equations introducing a magnetic scalar potential,  $\mathbf{H}_d = -\nabla U$ . The scalar potential follows from the magnetostatic boundary value problem

$$\nabla^2 U = \nabla \mathbf{M} \quad \text{inside the magnet,} \quad (15)$$

$$\nabla^2 U = 0 \quad \text{outside the magnet, and} \quad (16)$$

$$(\nabla U^{\text{in}} - \nabla U^{\text{out}}) \cdot \mathbf{n} = \mathbf{M} \cdot \mathbf{n} \quad \text{at the boundary with surface normal } \mathbf{n} \quad (17)$$

Equations (15) to (17) can be solved using a hybrid finite element / boundary element method (Fredkin et al. 1990). This method is especially useful for the simulation of the magnetostatic interactions of distinct magnetic elements, since no mesh is required outside the magnetic particles. The magnetic scalar potential is split into  $U = U_1 + U_2$ , where  $U_1$  accounts for the divergence of magnetization within the particle and  $U_2$  is required to meet the boundary conditions. The latter also carries the magnetostatic interactions between distinct magnetic particles.  $U_1$  is zero outside the particle and is the solution of the Poisson equation within the particle with the boundary condition,  $\nabla U_1 \cdot \mathbf{n} = \mathbf{M} \cdot \mathbf{n}$ . The potential  $U_2$  satisfies the Laplace equation everywhere and shows a jump at the surface of the particle. The computation of  $U$  consists of three steps:

1. A standard finite element method is used to solve Poisson's equation for  $U_1$ .
2. The potential  $U_2$  is calculated at the boundary:

$$\underline{U}_2 = \mathbf{B} \underline{U}_1,$$

$\mathbf{B}$  is a  $m \times m$  matrix which relates the nodes at the surface to each other and  $\underline{U}_1$  is the vector of the  $U_1$  values at the surface nodes. The matrix  $\mathbf{B}$  is dense and follows from the boundary element discretization of the double layer operator.

3. Once  $U_2$  at the boundary has been calculated, the values of  $U_2$  within the particles follow from Laplace's equations with Dirichlet boundary conditions, which again can be solved by standard finite element technique.

### 3.3. Time integration

After the evaluation of the magnetic moments and the effective fields at the nodes of the finite element grid a system of coupled ordinary differential equations has to be solved. In numerical micromagnetic simulations various time integrations method have been used.

In numerical micromagnetics the Runge Kutta method or Adams methods are suitable for weakly coupled systems (Mansuripur 1988, Zhu et al. 1989). Both are successfully used for the simulation of magnetostatically interacting grains in magnetic recording. Higher order backward differentiation formula (BDF methods) are most appropriate for ordinary differential equations resulting from the space discretization of a partial differential equations. Especially in highly exchange coupled system BDF methods are more efficient than explicit time integration schemes. BDF methods are implicit and thus require to solve a nonlinear system of equations at each time step. However, only a few Newton steps are required to obtain convergence. At each Newton step a linear system of equations has to be solved. Due to the long-range magnetostatic interactions, which couples all the nodes of the computational grid, the system matrix of this equation is fully populated. The use of a generalized minimum residual method (GMRES) avoids the storage of the system matrix. A considerable speed up for the solution of the linear system can be obtained with proper preconditioning.

The software package CVODE (Hindmarsh et al. 1995) provides a general framework to compare different time integration schemes. Fig. 4a gives the CPU time as a function of the simulated time during the magnetization reversal of a granular thin film element. Fig. 4b shows the remanent state and a snapshot during magnetization reversal. The dark areas are reversed domains. The comparison of the CPU time for different time integration schemes confirms that the preconditioned BDF method is faster than the Adams methods. For preconditioning an approximate Jacobian matrix is passed to CVODE which includes the exchange and anisotropy term but omits the magnetostatic contributions. Thus the approximate Jacobian remains sparse and can be calculated on the fly. Yang and Fredin (Yang et al. 1998) used similar approach to simulate magnetization reversal in ellipsoidal particles.

At finite temperature the noise term has to be taken into account. As shown by Garcia-Palacios and Lazaro (Garcia-Palacios, 1998) the equation has to be interpreted in the sense of Stratonovich, in order to obtain the correct thermal equilibrium properties. The numerical integration of the stochastic differential equation is performed using the method of Heun. For the pure deterministic case the Heun method reduces to the standard second order Runge-Kutta method (Kloeden et al. 1995). Numerical studies for simple spin systems confirmed that the Heun scheme is numerically more stable and allows larger time steps than the Euler or the Mil'shtein scheme (Scholz et al. 2001).

## 4. Numerical examples

Section 4.1 presents the magnetization reversal dynamics of small particles. Section 4.2 treats the hysteresis properties of granular thin film elements. Section 4.3 compares different reversal modes of circular nano-dots. The simulations in sections 4.1 to 4.3 are performed neglecting thermal fluctuations ( $T = 0$  K). The effects of thermal fluctuations on the magnetization reversal of magnetic nano-wires is discussed in section 4.4.

## 4.1. Small particles

If a magnetic particle is sufficiently small it will reverse by uniform rotation. Numerical experiments indicate that the dynamic properties obtained from the simulation of a finite particle and a single magnetic moment are quite similar. The switching dynamics were calculated for a columnar grain (Suess et al. 2001a) as used in perpendicular recording (Richter 1999) and are compared with the numerical results for a single spin. The geometry of such a grain can be seen in figure 5. The basal plane of the irregular pentagon has a diameter of 12 nm. We varied the column length (the height of the grain), denoted below by  $l_c$ . The material parameters are chosen for Co-Cr ( $\mu_0 M_s = 0.5$  T,  $A = 10^{-11}$  J/m,  $K_u = 3 \times 10^5$  J/m<sup>3</sup>). The easy axis is perpendicular to the basal plane. The Gilbert damping constant is  $\alpha = 0.01$ . If the length of the particle is smaller or equal 20 nm the reversal process is in uniform rotation. The external field is applied instantaneously at an angle of  $1^\circ$  off the easy axis.

Figure 5 compares the calculated switching time as a function of the applied field for the columnar particle and the single magnetic moment. The solid line with circles in figure 5 shows the switching time for the columnar grain with a column length of 20 nm and a damping constant  $\alpha = 0.01$  as a function of the field strength. We define switching time as the time until  $M_z$  crosses zero after the application of the external field. The switching times are calculated for external fields in the range of about  $-0.5 \times 2K_u/(\mu_0 M_s)$  to  $0.5 \times 2K_u/(\mu_0 M_s)$ . Since we neglect thermal activation in this investigation, no switching is possible if  $|\mathbf{H}_{\text{ext}}|$  becomes too low. It is conspicuous that the switching time does not decrease with increasing external field in the whole regime but shows a maximum slightly above the anisotropy field,  $2K_u/(\mu_0 M_s)$ . The switching time as a function of field strength for the single magnetic moment (circles in figure 5) strongly resembles that of the columnar grain and helps to understand the dependence of the switching time on the applied field.

Figure 6 shows the energy as a function of the  $x$  and  $y$  component of the magnetic moment just after the application of the external field of  $H_{\text{ext}} = -0.9 \times 2K_u/(\mu_0 M_s)$  and  $H_{\text{ext}} = -1.3 \times 2K_u/(\mu_0 M_s)$ , respectively. Before the application of the external field, the system is in equilibrium at  $M_x = M_y = 0$  marked with a black dot in the top and the bottom picture of figure 3. If a field is applied instantaneously the energy landscape suddenly changes. The system is no longer in equilibrium. In the case of  $H_{\text{ext}} = -1.3 \times 2K_u/(\mu_0 M_s)$  a well defined maximum is formed because the Zeeman energy dominates the total energy. Due to the small damping constant in the LLG equation, the magnetization moves along a path with almost constant energy around the maximum of the energy surface. During this motion the angle between the magnetization and the external field remains small. More precisely the angle between  $\mathbf{M}$  and  $-\mathbf{H}_{\text{ext}}$  (parallel to the  $z$  direction) is small during the initial motion of the magnetization. Thus the corresponding torque is small. The relaxation towards the reversed state is slow. The switching time is long. If the external field is comparable with the anisotropy field, the energy landscape is more complex. The anisotropy energy and Zeeman energy contribute in the same order of magnitude to the total energy. A path with nearly constant energy is no longer a circle. The angle between  $\mathbf{M}$  and  $-\mathbf{H}_{\text{ext}}$  becomes higher (figure 6, top) which leads to a high torque. The high torque leads to a fast relaxation towards the reversed state. Fast switching modes are possible if

the rise time of the external field is shorter than the relaxation of the magnetization towards the local minimum close to the initial state.

In addition, Figure 5 gives the switching time calculated for a single magnetic moment at  $T = 300$  K. The magnetic moment corresponds to a magnetic particle with a volume of  $(12 \text{ nm})^3$  and a spontaneous polarization  $\mu_0 M_s = 0.5$  T. The results at finite temperature have been averaged over 100 simulations. The solid line in figure 5 shows that fast switching at low external fields also occurs at 300 K. However, the finite temperature reduces the switching time. In the investigated temperature range (0 K - 400 K) the switching time decreases almost linearly as a function of the temperature. The fluctuation of the magnetization are responsible for the reduction of the switching time at non-zero temperature. At non-zero temperature the number of precessions until  $M_z$  reaches zero is smaller than at  $T = 0$ . This indicates that the system at non-zero temperature is effectively stronger damped. The thermal field causes fluctuations of the magnetic moment orientation. If the applied field is almost parallel to the anisotropy axis, the thermal fluctuations always increase the angle between the magnetic moment and the effective field which causes a higher torque.

#### 4.2. Thin film elements

Thin film magnetic elements are the basic structural units of magnetic memory cells and magnetic sensors. A precise understanding of the switching process and the possible tuning of the switching field and the switching time are helpful for the future development of these devices. Magnetic nano-elements are found to reverse by the formation of vortices, which in turn leads to the expansion of the domain which has its magnetization parallel to the external field. Vortices may nucleate from end domains which are formed in the remanent state to minimize the magnetostatic energy (Kirk et al. 1997). An additional source for vortex nucleation are surface irregularities and grain boundaries. Numerical micromagnetic simulations show that edge roughness and the polycrystalline microstructure considerably lower the switching field of Co elements (Schrefl et al. 1999).

Figure 7 gives the microstructure of the polycrystalline sample and transient states during irreversible switching. The competitive effects of shape and random crystalline anisotropy lead to a magnetization ripple structure. Sharp edge irregularities help to create vortices, which will move through the width of the element. This process starts at a reversed field of  $H_{\text{ext}} = -95$  kA/m and leads to the reversal of on half of the particle. In what follows, a second vortex forms and the entire Co-element becomes reversed. In granular Co elements with random magneto-crystalline anisotropy, vortices form immediately after the application of a reversed field. For zero magnetocrystalline anisotropy a vortex breaks away from the edge only after a waiting time of about 0.8 ns. The coercive field of the flat element without surface roughness and grain structure was found to be 140 kA/m.

### 4.3. Circular nano-dots

The reversal process of circular nano-dots strongly depends on the diameter and the thickness of the dots (Suess et al. 2001b). The larger the dots, the more nonuniform reversal modes are observed. In addition a small Gilbert damping constant favors nonuniform reversal in comparison to a large damping constant. Figure 8 shows the finite element mesh at the surface of a circular nano-dot. The calculations were performed for NiFe ( $K_u = 0$ ,  $\mu_0 M_s = 1$  T,  $A = 10^{-11}$  J/m).

Figure 8 shows transient states during reversal for different sizes of the magnetic nano-dot. A damping constant  $\alpha = 1$  was used. The left dot has a diameter of 55 nm and a thickness of 10 nm. For this small volume of the particle the reversal process is homogenous rotation. The middle dot shows the reversal process of a dot with  $d = 110$  nm and a thickness of 10 nm. A s-state is formed which reduces magnetic surface charges and hence the magnetostatic energy. If the thickness exceeds 15 nm, as in the right picture, a vortex state has smaller energy than an s-state. Two reasons can be mentioned why thicker samples favor the formation of a vortex state. First, in the core of a vortex state the magnetization points perpendicular to the surface and produces a demagnetizing field. With increasing thickness the demagnetizing field decreases which reduces the magnetostatic energy. Secondly, the surface charges at the cylindrical surface which lead to a high magnetostatic energy become dominant with increasing thickness.

In addition, the Gilbert damping constant was found to influence the reversal process. Decreasing the damping constant may change the reversal mode from nonuniform rotation to vortex motion. Figure 9 compares the time evolution of the magnetic component parallel to the field for  $\alpha = 1$  and  $\alpha = 0.01$  (diameter  $d = 220$  nm and thickness  $t = 10$  nm). After the application of a field  $H_{\text{ext}} = -8$  kA/m,  $1^\circ$  off the  $x$ -direction, the torque remains small. For  $\alpha = 1$  the nanodot starts to switch only after a waiting time of about 3 ns. For  $\alpha = 0.01$  the waiting time reduces to about 0.5 ns. Leineweber und Kronmüller (Leineweber et al. 1999) observed that a certain waiting time is required before switching is initiated in hard magnetic spheres. The insets compare two transient states during reversal. Whereas for  $\alpha = 1$  the magnetization reverses nonuniformly, two vortices are formed at the beginning of the reversal process for  $\alpha = 0.01$ .

### 4.4. Magnetic nano-wires

The nucleation and reversal of reversed domains in magnetic nano-wires was studied at non-zero temperatures. The energy barriers and the activation volume were derived from the numerical results. The diameter of the wire Co wire was 2 nm. The intrinsic magnetic properties of Co ( $\mu_0 M_s = 1.76$  T,  $A = 1.3 \cdot 10^{-11}$  J/m,  $K_u = 6.8 \cdot 10^5$  J/m<sup>3</sup>) and a Gilbert damping constant  $\alpha = 1$  were assumed for the calculations. The magneto-crystalline anisotropy direction was assumed to be parallel to the long axis of the wire.

Wires with a length smaller than 16 nm were found to reverse by uniform rotation. Fig. 10 shows schematic diagrams of the energy barrier as a function of the angle with

respect to the easy axis. An external field lowers the energy barrier. From the calculated relaxation time,  $\tau$ , the energy barrier can be derived numerically fitting the numerical results to

$$\mathbf{t} = f_0^{-1} \exp\left(\frac{E_B}{k_B T}\right), \quad (18)$$

where  $f_0$  is the attempt frequency. The energy barrier increases with increasing volume of the wire as long as the reversal mode is uniform rotation. The numerically derived energy barrier for uniform rotation agrees well with the result obtained from the Stoner-Wohlfarth theory (Street et al. 1999).

$$E_B(H_{\text{ext}}) = KV \left(1 - \frac{H_{\text{ext}}}{H_K}\right)^2, \quad H_K = \frac{2\mathbf{m}_0 K}{M_s}, \quad (19)$$

where  $K$  is the effective anisotropy constant taking into account the magnetocrystalline anisotropy and the shape anisotropy of the wire.

Wires with a length of 32 nm reverse by the nucleation and expansion of reversed domains. Now the energy barrier is independent of the wire length, since the nucleation process starts at the wire ends where a strong demagnetizing initiates magnetization reversal. Once the reversed domain has formed it expands over the entire wire. Figure 11 illustrates this process. An effective activation volume,  $v$ , can be derived from the energy barrier under the assumption that the activation energy corresponds to the energy of the nucleus of reverse magnetization (Street et al. 1999)

$$E_B(H_{\text{ext}}) = -v\mathbf{m}_0 M_s H_{\text{ext}}. \quad (20)$$

The activation volume can be derived from the slope of the  $E_B(H_{\text{ext}})$  curve

$$v = -\frac{1}{\mathbf{m}_0 M_s} \frac{\partial E_B}{\partial H_{\text{ext}}}. \quad (21)$$

Fig. 12 gives the calculated energy barrier for a 1:16 aspect ratio nano-wire as a function of the external field. The dashed line corresponds to the analytical result obtained by Braun (Braun 1994). The numerical values for the energy barrier are about factor of 2-3 smaller than those derived analytically. This may be attributed to inhomogeneous magnetic states which neglected in the analytical model. The numerically-obtained energy barrier depends linearly on the applied field, which indicates that the reversal takes place by the formation of a nucleus of reverse magnetization at one end of the wire. The activation volume was derived to be  $v = (2.1 \text{ nm})^3$  which approximately corresponds to the cube of the wire diameter. Li and co-workers (Li et al. 1997) obtained a similar result from magnetic measurements on  $\alpha$ -Fe nanowires.

## Acknowledgment

Work supported by the Austrian Science Fund (Y132 PHY, P13260-TEC).

## References

- Braun, H.-B., J. Appl. Phys. **76**, 6310 (1994).
- Brown, W. F., Jr., Micromagnetics, (New York, Wiley, 1963).
- Brown, W. F., Jr, IEEE Trans. Magn. **15**, 1196 (1979)
- Dahlberg, E. D. and J. G. Zhu, Physics Today **48**, 34, (1995).
- Fredkin, D. R. and T. R. Koehler, IEEE Trans. Magn. **26**, (415) 1990.
- García-Palacios, J. L. and F. J. Lázaro, Phys. Rev. B **58**, 14937 (1998).
- Gilbert, T. L., Phys. Rev. **100**, 1243 (1955).
- Hertel, R. and H. Kronmüller, IEEE Trans. Magn. **34**, 3992 (1998)
- Hindmarsh, A. C. and L. R. Petzold, Computers in Physics **9**, 148 (1995).
- Kikuchi, R., J. Appl. Phys. **27**, 1352 (1956).
- Kirk, K. J., J. N. Chapman and C. D. W. Wilkinson, Appl. Phys. Lett **71**, 539 (1997).
- Kloeden, P. E. and E. Platen, Numerical Solution of Stochastic Differential Equations, (Berlin, Heidelberg, Springer, 1995).
- Leineweber, T. and H. Kronmüller, J. Magn. Magn. Mater. **192**, 575 (1999).
- Li, F. L., R. M. Metzger and W. D. Doyle, IEEE Trans. Magn. **33**, 4423 (1997).
- Mansuripur, M., J. Appl. Phys. **63**, 5809 (1988).
- Prinz, G. A., J. Magn. Magn. Mater. **200**, 57 (1999).
- Ramstöck, K., T. Leibl, A. Hubert, J. Magn. Magn. Mater. **135**, 97 (1994).
- Rave, W., K. Ramstock and A. Hubert, J. Magn. Magn. Mater. **183**, 329 (1998).
- Richter, H. J., J. Phys. D: Appl. Phys. **32**, 147 (1999).
- Schrefl, T., J. Magn. Magn. Mater. **207**, 45 (1999).
- Schrefl, T., J. Fidler, K. Kirk and J. N. Chapman, J. Appl. Phys. **85**, 6169 (1999).
- Scholz, W., T. Schrefl and J. Fidler, J. Magn. Magn. Mater. **196-197**, 933 (1999).
- Scholz, W., D. Suess, T. Schrefl and J. Fidler, Computational Materials Science **18**, 1 (2000).
- Scholz, W., T. Schrefl and J. Fidler, J. Magn. Magn. Mater. **233**, 296 (2001).
- Street, R., and D. C. Crew, IEEE Trans. Magn. **35**, 4407 (1999).
- Suess, D., T. Schrefl and J. Fidler, IEEE Trans. Magn. **37**, 1664 (2001a).
- Suess, D., T. Schrefl, J. Fidler and V. Tsiantos, IEEE Trans. Magn. **37**, 1690 (2001b).
- Terris, B. D., L. Folks, J. E. E. Baglin, A. J. Kellock, H. Rothuizen, P. Vettinger, App. Phys. Lett. **75**, 403 (1999).
- Yang, B. and D. R. Fredkin, IEEE Trans. Magn. **34**, 3842 (1998).
- Zhu, J.-G. and H. N. Bertram, J. Appl. Phys. **66**, 1291 (1989).

## Figure captions

- Fig. 1. Basic micromagnetic contributions to the effective field.
- Fig. 2. Motion of the magnetization towards equilibrium. (a) High damping, (b) low damping, and (c) low damping at non-zero temperature.
- Fig. 3. Schematics of the space discretization: (a) Tetrahedral finite element mesh of a granular thin film. The region of fine mesh results from adaptive refinement near a domain wall. (b) Box volumes and node points.
- Fig. 4. Magnetization reversal of a granular thin film element. (a) CPU time as a function of the simulated time. (b) Transient magnetic states during switching.
- Fig. 5. Top: Small columnar Co-Cr particle. Bottom: switching time as a function of the field strength. Circles: single magnetic moment at zero temperature. Solid line: single magnetic moment  $T = 300$  K. Solid line with circles: columnar grain at zero temperature.
- Fig. 6. Energy landscape as a function of  $M_x$  and  $M_y$ . The bold line shows the path of the magnetic polarization after the application of an external field of (top)  $H_{\text{ext}} = -0.9 \times 2K_u/(\mu_0 M_s)$  and (bottom)  $H_{\text{ext}} = -1.3 \times 2K_u/(\mu_0 M_s)$ . The black dots show the initial state.
- Fig. 7. Microstructure of the polycrystalline sample and snapshots of the magnetization distribution at different times after the application of an applied field of  $H_{\text{ext}} = -95$  kA/m.
- Fig. 8. Top: Finite element model of one circular nano-dot. The triangles show the surface mesh used for the boundary element method. Bottom: Three possible reversal modes (rotation: diameter  $d = 55$  nm, thickness  $t = 10$  nm; nonuniform:  $d = 110$  nm,  $t = 10$  nm; vortex:  $d = 110$  nm,  $t = 15$  nm).
- Fig. 9. Time evolution of the magnetic polarization parallel to the external field for different values of the damping constant  $\alpha$  ( $d = 220$ ,  $t = 10$  nm).
- Fig. 10. Energy of a small particle as a function of the angle between the easy axis and the magnetization. (a) zero external field and (b) reversed applied field.
- Fig. 11. Nucleation and expansion of reversed domains in Co nanowires with an aspect ratio of 1:16.
- Fig. 12. Energy barrier as a function of the applied field. The open symbols give the numerical values. The dotted line is a linear fit of the numerical values. The dashed line gives the analytic result according to (Braun 1994).



Fig. 1.

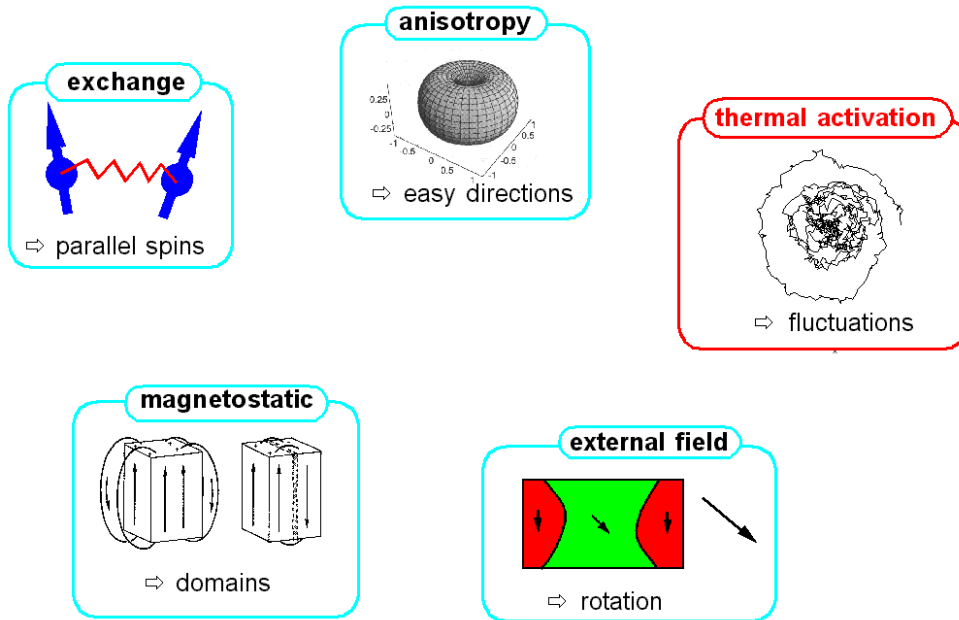


Fig. 2

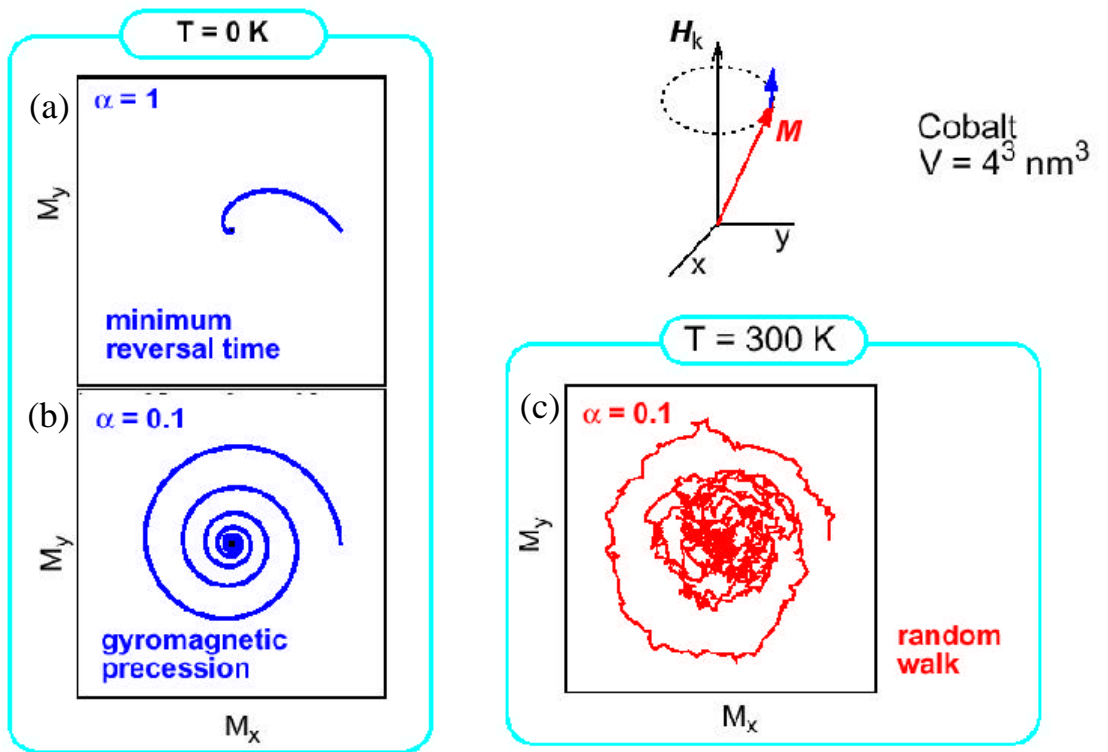


Fig. 3.

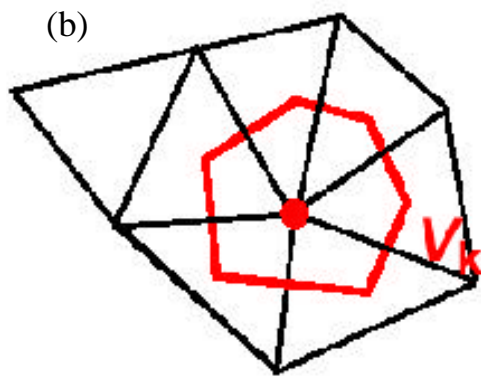
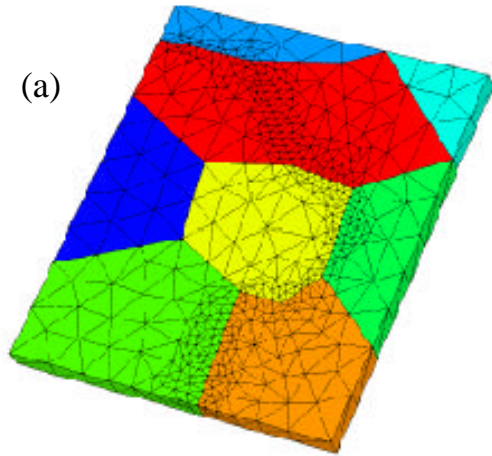


Fig. 4.

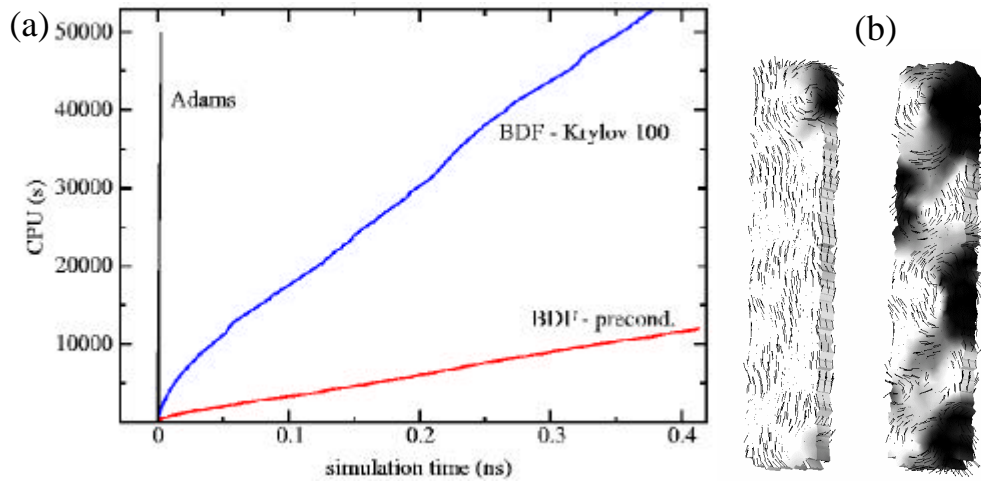


Fig. 5.

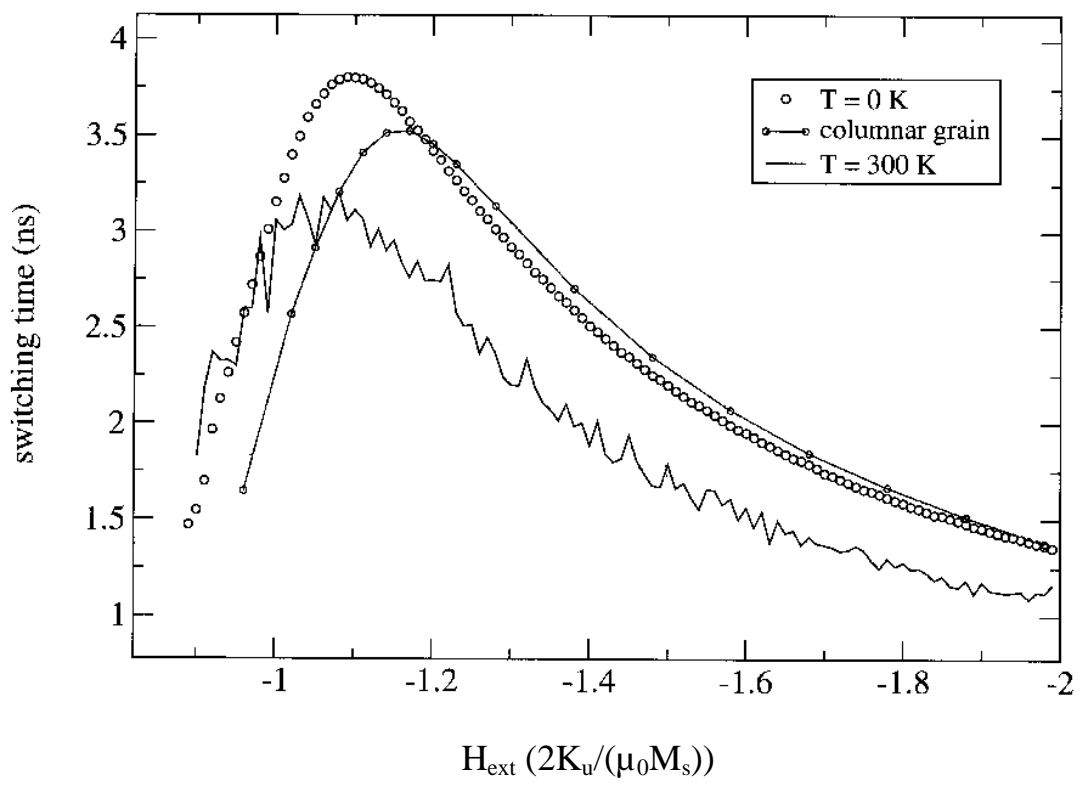
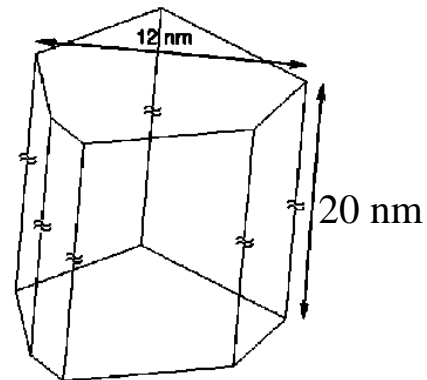


Fig. 6.

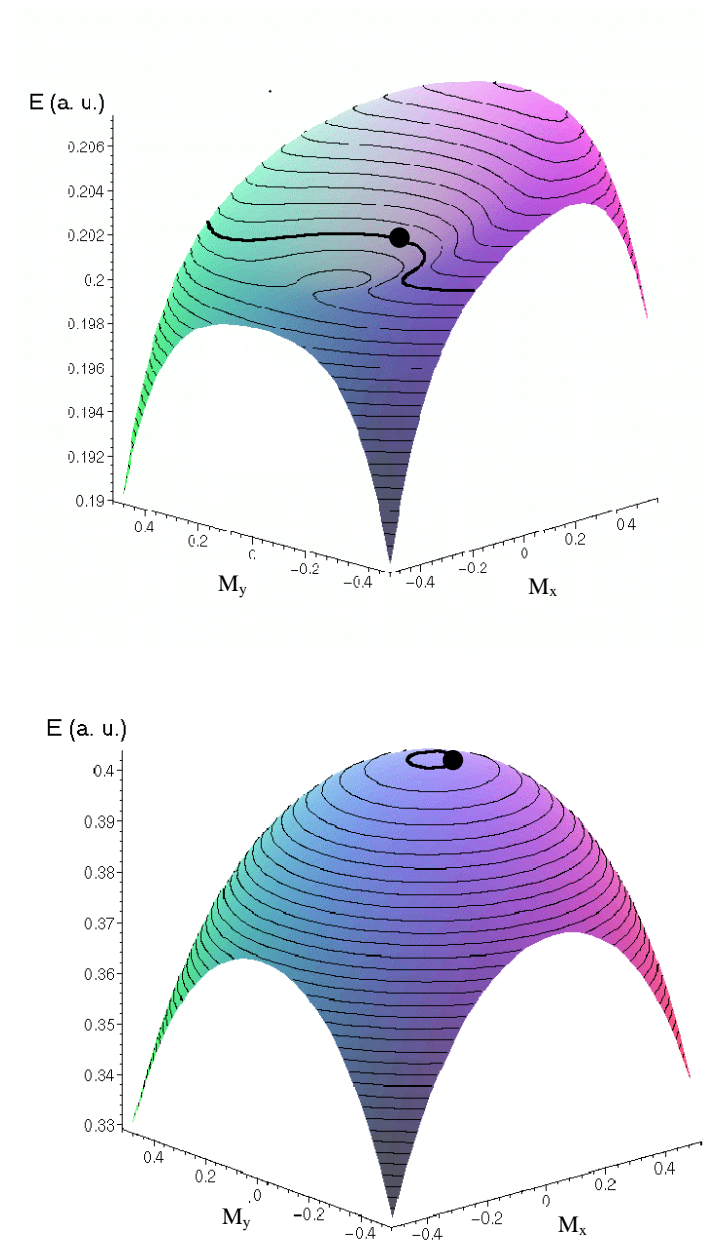


Fig. 7.

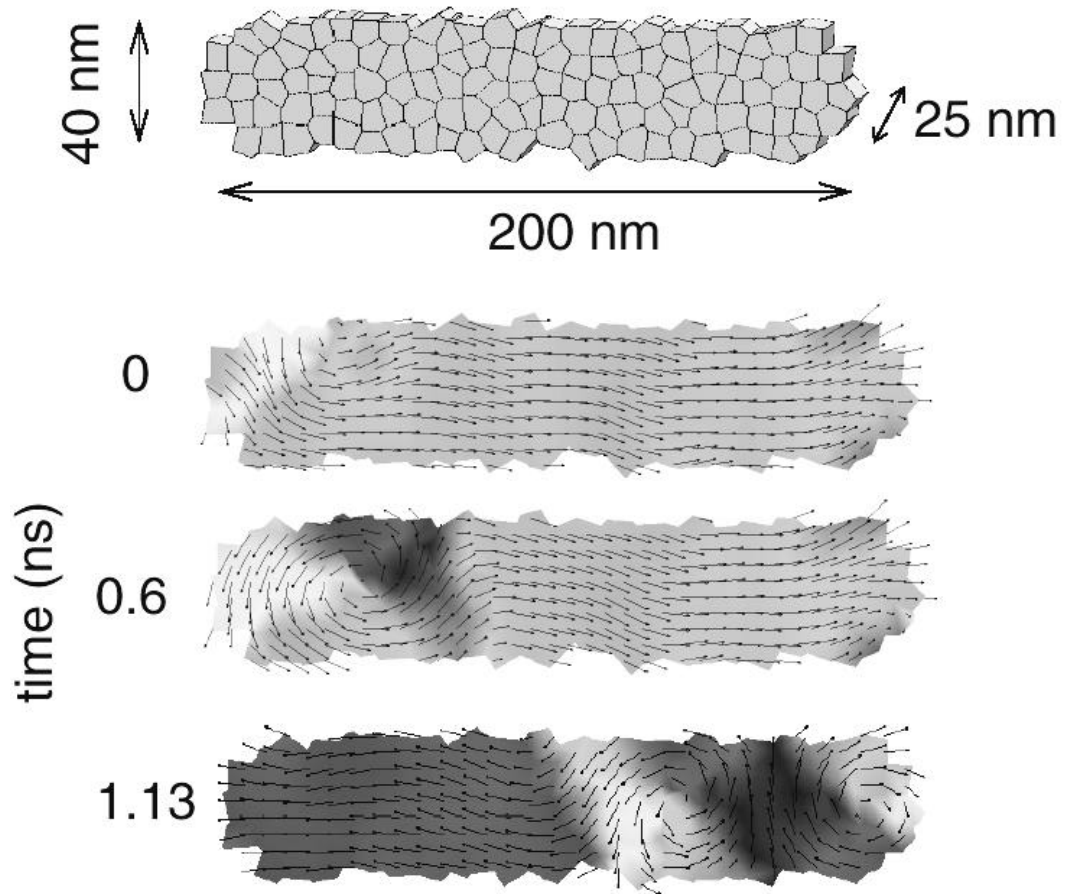


Fig. 8.

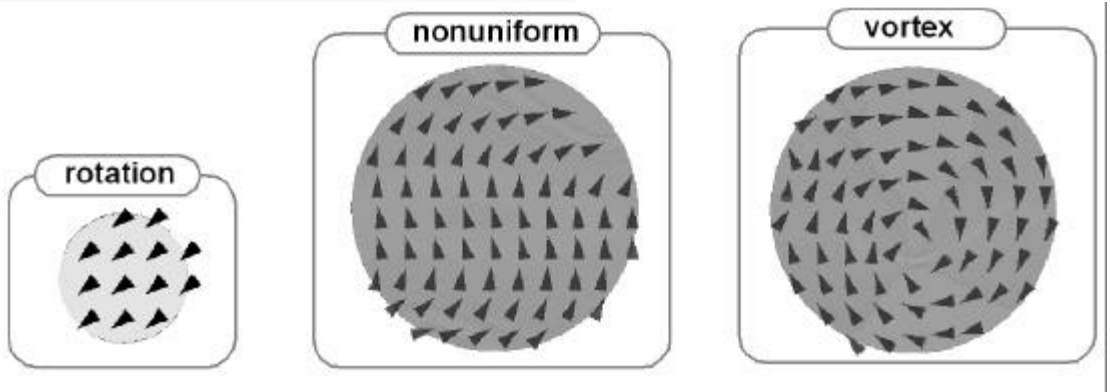
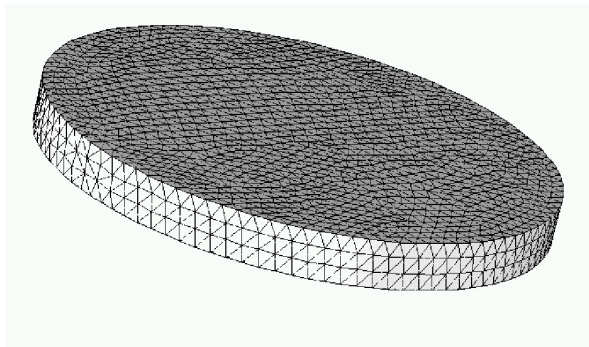


Fig. 9.

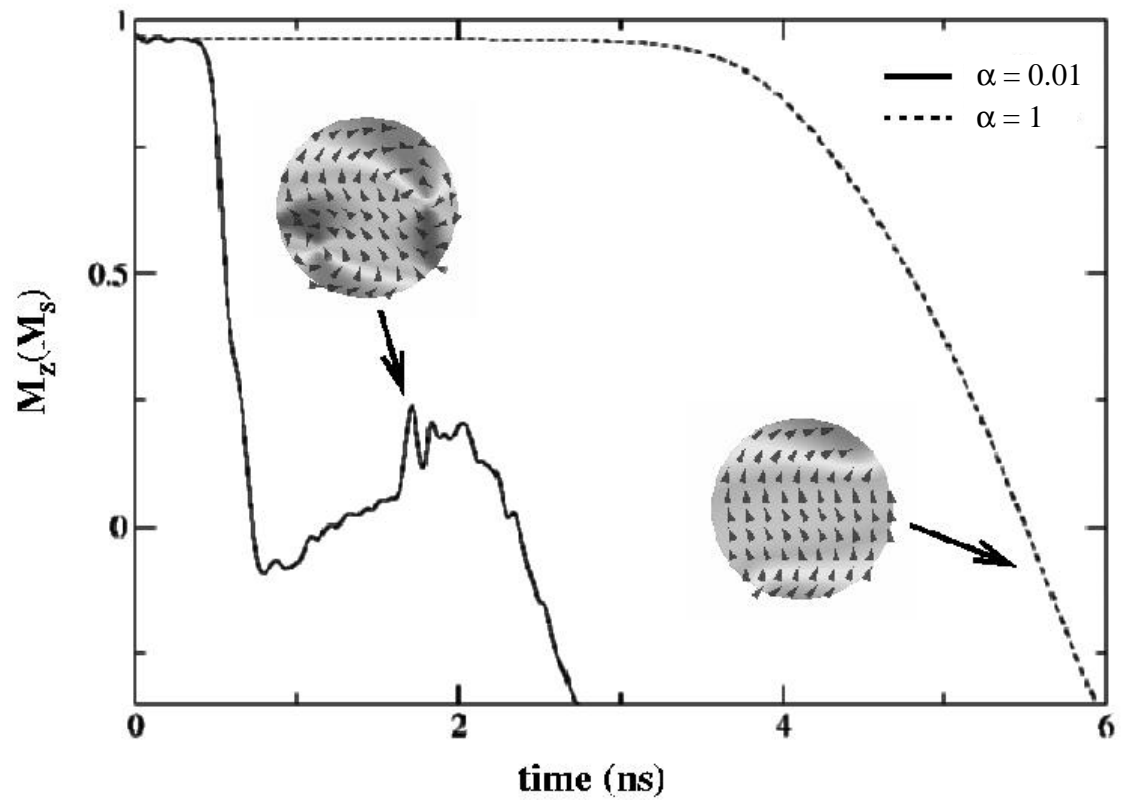


Fig. 10

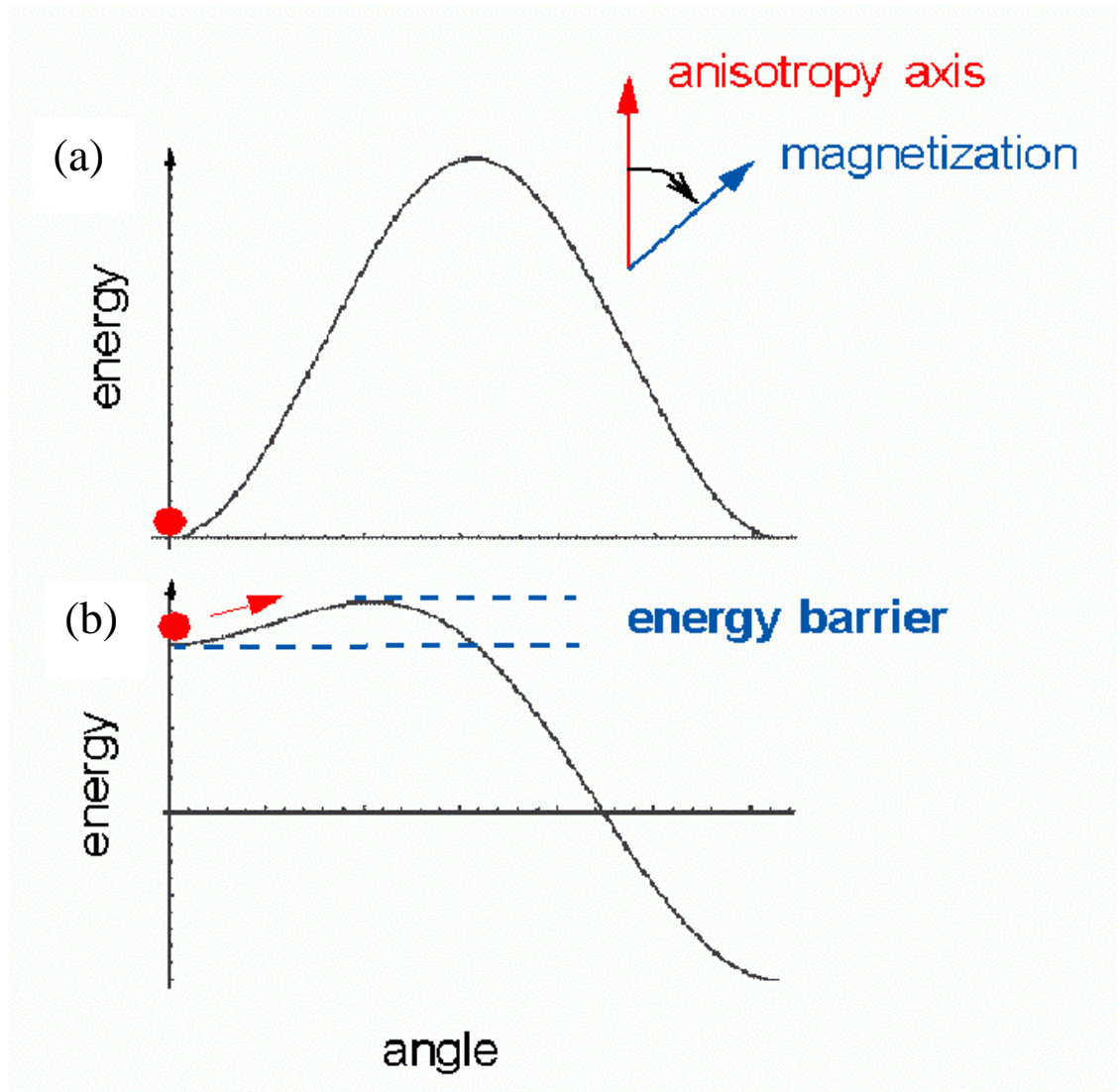


Fig. 11

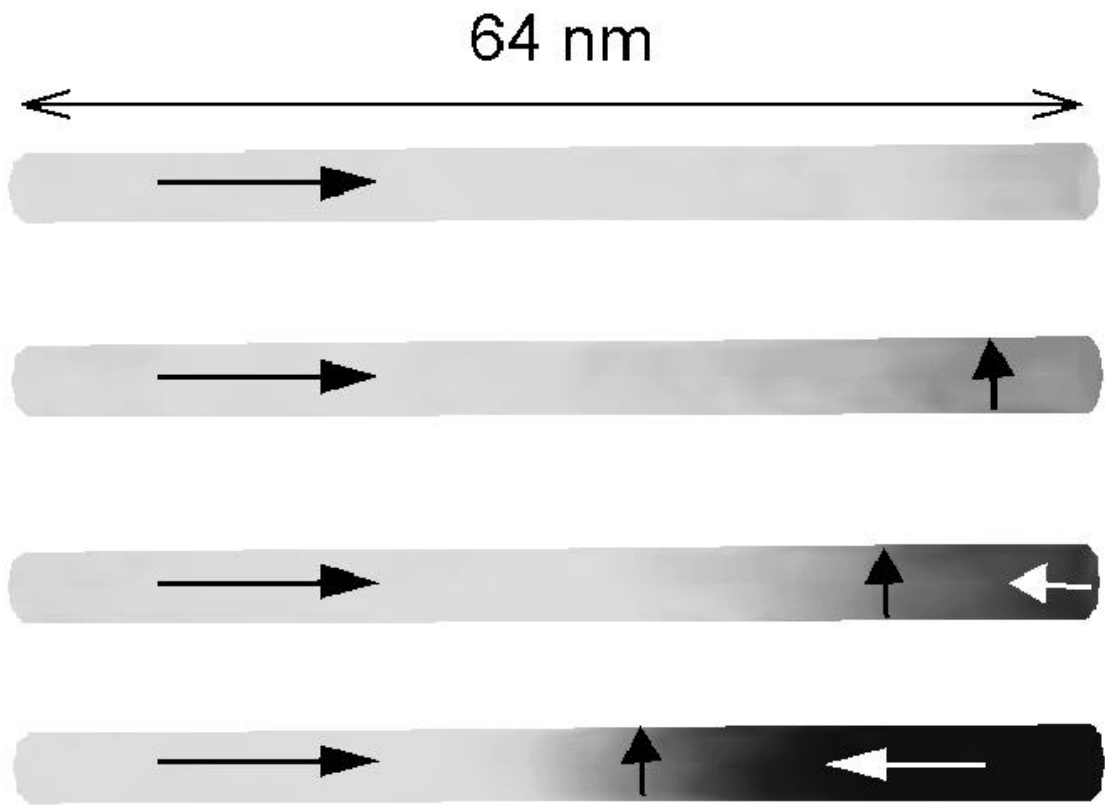


Fig. 12.

